Fuel 370 (2024) 131743

Contents lists available at ScienceDirect

Fuel

journal homepage: www.elsevier.com/locate/fuel

Full Length Article

On the inaccuracies of point-particle approach for char conversion modeling

Thamali R. Jayawickrama [a], Nils Erland L. Haugen [a,b], Kentaro Umeki [a,c,*]

[a] Energy Engineering, Div. Energy Science, Luleå University of Technology, 971 87 Luleå, Sweden
[b] Department of Thermal Energy, SINTEF Energy Research, Kolbjørn Hejes vei 1 A, 7491 Trondheim, Norway
[c] Technical University of Munich, Chair of Energy Systems, Boltzmannstr. 15, 85748 Garching b. München, Germany

ARTICLE INFO

Keywords:
Char gasification
Point-particle method
Particle-resolved simulation
Stefan flow

ABSTRACT

Char conversion is a complex phenomenon that involves not only heterogeneous reactions but also external and internal heat and mass transfer. Reactor-scale simulations often use a point-particle approach (PP approach) as sub-models for char conversion because of its low computational cost. Despite a number of simplifications involved in the PP approach, there are very few studies that systematically investigate the inaccuracies of the PP approach. This study aims to compare and identify when and why the PP approach deviates from resolved-particle simulations (RP approach). Simulations have been carried out for CO_2 gasification of a char particle under zone II conditions (*i.e.,* pore diffusion control) using both PP and RP approaches. Results showed significant deviations between the two approaches for the effectiveness factor, gas compositions, particle temperature, and particle diameter. The most significant sources of inaccuracies in the PP approach are negligence of the non-uniform temperature inside the particle and the inability to accurately model external heat transfer. Under the conditions with low effectiveness factors, the errors of intra-particle processes were dominant while the errors of external processes became dominant when effectiveness factors were close to unity. Because it assumes uniform internal temperature, the models applying the PP approach always predict higher effectiveness factors than the RP approach, despite its accurate estimation of intra-particle mass diffusion effects. As a consequence, the PP approach failed to predict the particle size changes accurately. Meanwhile, no conventional term for external heat transfer could explain the inaccuracy, indicating the importance of other sources of errors such as 2D/3D asymmetry or penetration of external flows inside the particles.

1. Introduction

Biomass is a source of renewable energy that is carbon neutral since it absorbs CO_2 from the atmosphere during photosynthesis. Therefore, it is an attractive option for replacing fossil fuels to mitigate climate change effects. However, biomass is cumbersome to use directly as a source of energy. Gasification is a convenient way of utilizing biomass and other solid fuels since the gas produced from the process has a wide range of applications. Entrained flow gasification has the highest share of large-scale gasifiers of coal in the world [1], and the process can produce high-quality syngas, which is favourable for the synthesis of biofuel [1–3]. However, entrained flow biomass gasification (EFBG) is still not available at the industrial level due to some barriers. Apart from economic challenges, major technical challenges of EFBG technologies include biomass feeding at elevated pressures, formation of smoothly flowing slags, and the elimination of incomplete carbon conversion in the form of char and soot [2,4].

One way to study gasification is by using numerical simulations. A major challenge of numerical simulations is the large variation of time and length scales existing in the gasification process. As an example, particle sizes are very small ($\mathcal{O}(10^{-6} - 10^{-3})$ m) compared to the reactor size ($\mathcal{O}(10^{0} - 10^{1})$ m) of an entrained-flow gasifier. Due to the wide gap, not only in length scales but also in time scales, fully resolved simulations of entire gasifiers are not practical with contemporary computational resources and methods. For a recent review of numerical approaches related to numerical simulations of coal conversion, please see [5]. In entrained flow biomass gasification, particles are suspended in the fluid, and the particles can therefore interact with the fluid or neighbouring particles through momentum, heat, and mass transfer. The current state-of-the-art is to use sub-grid models to mimic small-scale phenomena (such as particle–fluid interactions) such that larger mesh sizes and time steps can be used. Therefore, the fidelity of simulations is highly dependent on the accuracy of the sub-grid models. One such modelling approach is the so-called point-particle (PP) approach, where every particle is considered as a point in space (occupying zero volume). The momentum, heat, and mass transfer between a particle and the fluid are calculated through drag coefficient (C_D),

* Corresponding author.
E-mail addresses: thamalirajika@gmail.com (T.R. Jayawickrama), kentaro.umeki@ltu.se (K. Umeki).

https://doi.org/10.1016/j.fuel.2024.131743
Received 15 November 2023; Received in revised form 28 February 2024; Accepted 19 April 2024
Available online 2 May 2024

Nusselt number (Nu), and Sherwood number (Sh) models, respectively. Furthermore, the rates of heterogeneous reactions are calculated as a product of intrinsic reaction rates and the effectiveness factor, which accounts for the effects of internal mass diffusion limitation. Here, it is essential to have models to calculate the variation of particle diameter, density, and evolution of internal particle surface area with the progress of the heterogeneous reactions. On the other hand, the variation of properties such as temperature and gas compositions throughout the particles is neglected in the PP approach.

The most widely used constitutive models for C_D, Nu and Sh of a particle immersed in a bulk fluid were developed under simplified conditions, such as non-porous particle, isothermal conditions, neglecting neighbour particle effects, and neglecting effects of Stefan flow [6–8]. Recently, a lot of improvements have been made to the models for C_D [9–11], Nu [9,11,12] and Sh [13] in terms of different shapes, the effect of porosity, the effect of Stefan flow, and effect of neighbouring particles. However, most recent works such as [14–17] still consider the constitutive models with an improvement for Stefan flow effects based on a model developed in a quiescent environment. More surprisingly, no previous study has considered additional transport mechanisms in the boundary layer, such as Stefan flow-driven advection and Dufour effects [18]. Therefore, it is vital to know how these models perform for the simulation of reactive particles in convective flows using PP approaches. It is especially important for model improvements to elucidate under which conditions the models with the PP approach fail and the reasons for deviations. Such studies are possible only through the comparison of the results from the PP approach with results produced from fully particle-resolved simulations (both particle interiors and the boundary layer), which are rare in the literature. Hereafter, we call such an approach a resolved-particle (RP) approach.

Char gasification is the rate-limiting step during gasification. Apart from that, char gasification usually occurs in Zone II, where the gasification reaction is controlled by both pore diffusion inside the char particle and chemical kinetics [19–21]. This makes the gasification process harder to model in comparison with Zone I and Zone III. Zone I is where the reaction rate is controlled by chemical kinetics (diffusion is fast and thus negligible). Therefore, the reaction rate can be modelled solely by the kinetics rate. The particle density is varying and the diameter of the particle is constant throughout reactions. Zone III is where the reaction rate is controlled by diffusion. Here, the reaction rates are fast compared to the diffusion rates, such that reactions occur only at the surface of the particle. Therefore, the density is constant, and the particle shrinks due to reactions. Hence, in Zone III, the reaction rate can be modelled by the mass transfer coefficient at the external surface of the particle. In Zone II, both particle diameter and density decrease with the progress of the reactions. The apparent reaction rate of a char particle in Zone II depends on many parameters, such as particle size, porosity, pore size distribution, diffusion rates of the gases into the pores, and intrinsic reaction rate [22]. Therefore, detailed studies of char conversion in Zone II would provide deeper insights into important parameters and modelling approaches. Detailed information about the three-zones can be found in [5].

When utilizing the PP approach simulating char conversion, there are two main categories of inaccuracies involved in the simulations. The first inaccuracy is the lack of knowledge of the exact chemical and physical properties of the char. For example, the thermal conductivity of char depends on the nanostructures (curvature, stack distance, and connectivity) of defected graphene-like aromatic planes and μm-scale pore-structure alignment. These structures are unique for each material and keep changing during the reactions, meaning it is not realistic to have precise knowledge of these parameters. The second inaccuracy is due to the fact that the particle interior, and the boundary layer surrounding the char particles, are not resolved but have to be modelled. While the former of these two categories of inaccuracies is related to how well the fuel is characterized, and how precisely the models we use to describe these chemical and physical properties can be fitted to experimental measurements, the latter category of inaccuracies is purely numerical. Hence, the latter category is not affected by shortcomings of material characterization or fitting with experiments. Which of the two inaccuracies is dominating is highly case-specific and cannot be determined a-priori. For the remainder of this paper, the focus will be purely on the latter of the two categories of inaccuracies.

Table 1
List of parameters that were varied for different simulation cases. Effectiveness factor (η), particle Reynolds number (Re), and Stefan Reynolds number (Re_{Sf}) are the values estimated from the results of the resolved particle simulation.

Case	T_∞ (K)	p_∞ (atm)	d_p (μm)	U_∞ (m/s)	$Y_{CO_2,\infty}$ (-)	η	Re	Re_{Sf}
1	1999	1.807	189.3	0.45	0.512	0.23	0.5	0.09
2	1999	1.807	189.3	2.70	0.512	0.44	3.0	0.03
3	1851	4.201	442.6	0.44	0.512	0.21	3.0	0.04
4	1891	4.506	97.21	0.32	0.512	0.74	0.5	0.08
5	1891	4.506	97.21	1.93	0.512	0.69	3.0	0.02
6	1735	7.672	228.1	0.32	0.99	0.58	3.0	0.03

As stated above, the objective of this study is to identify and quantify the origins of inaccuracies in the point-particle approach for char gasification modelling. First, we carried out resolved-particle simulations of char particle gasification under different conditions. Both the exterior and interior of the particle are resolved. A non-equimolar gasification reaction is considered to create a Stefan flow. The results of simulations were compared with the modelling results from the point-particle approach. Then, we identified the differences between the two approaches and the reasons behind the differences and suggested improvements of the point-particle approaches.

2. Methodology

2.1. Simulation case setup

Fig. 1 shows the overall arrangement of the simulation cases. Char gasification in entrained flow biomass gasification (EFBG) process is considered as a case study. More details about char gasification modelling can be found in these Refs. [19,20,22]. This work only considers the non-equimolar Boudouard reaction ($C + CO_2 \rightarrow 2CO$) as a representative gasification reaction for simplicity. The char particle is modelled as a porous medium (See Fig. 1). Since there is no oxygen in the simulation domain, gas-phase reactions are neglected.

In EFBG, pulverized particles are suspended in the bulk gas with particle volume fractions below 0.001. Therefore, the simulation is set up to be an isolated particle immersed in a uniform, non-isothermal bulk gas flow. Here, uniform bulk flow means that, far upstream of the particle, the bulk fluid flow has uniform properties, such as velocity, pressure, temperature and other thermo-physical properties of the fluid, both with respect to time and space. Particle diameters and slip velocities in EFBG vary within the range of <1 mm and $0.1-3\ \mathrm{ms}^{-1}$, respectively [23]. Therefore, the same ranges of parameters are used for this work as summarized in Table 1.

Three non-dimensional numbers, namely, particle Reynolds number, Stefan Reynolds number, and the effectiveness factor are considered in Table 1. Here, particle Reynolds number (Re) is defined as:

$$\mathrm{Re} = \frac{\rho_g U d_p}{\mu}, \tag{1}$$

where U is the relative velocity between the particle and the bulk flow, ρ_g is fluid density, μ is fluid viscosity and d_p is particle diameter. Stefan Reynolds number ($\mathrm{Re}_{\mathrm{Sf}}$) is defined by the same formula, but the velocity of Stefan flow is used in place of the relative velocity. The effectiveness factor (η) is defined as:

$$\eta = \frac{\dot{m}_{c,tot}}{\dot{m}_{c,surf}}, \tag{2}$$

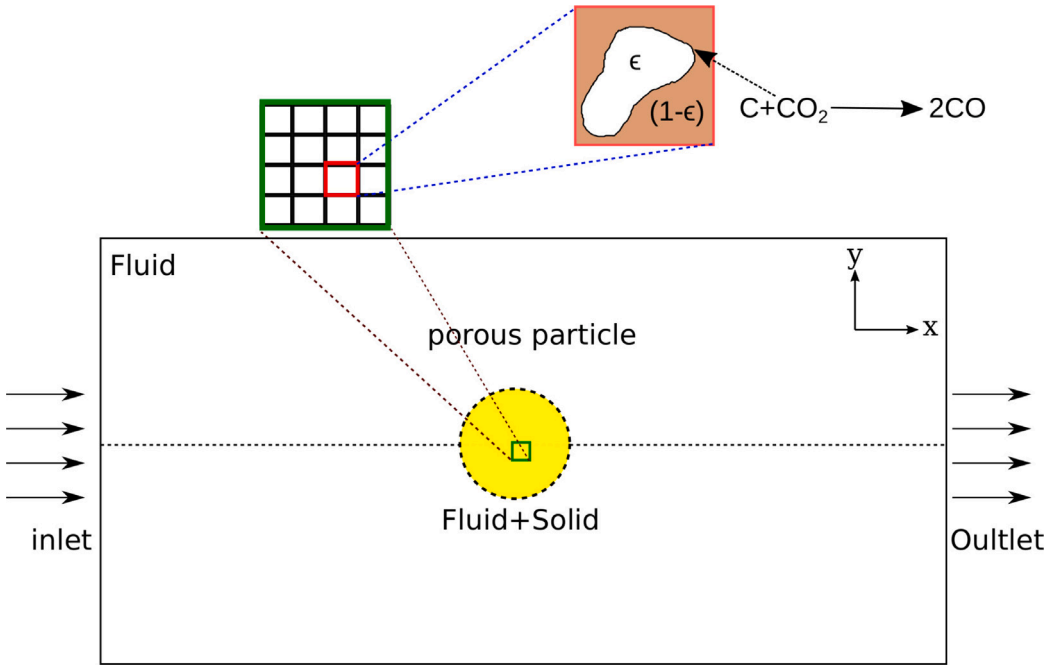

Fig. 1. Overview of the simulation domain.

where $\dot{m}_{c,tot}$ is the actual conversion rate of the char particle, while $\dot{m}_{c,surf}$ is the char conversion rate the particle would experience if the entire particle had a reaction rate equal to that at the surface.

The values of 0.5 or 3 are chosen for the Reynolds number, while the effectiveness factor (η) is either considered as low; 0.2–0.3 (cases 1–3) or high; 0.6–0.7 (cases 4–6). Note that the exact effectiveness factor or Stefan Reynolds number was not possible to estimate in advance due to uncertainties in the existing analytical models. Therefore, the values shown in Table 1 were taken from the results of particle-resolved simulation.

Particle Reynolds numbers considered here are equal to or less than 3. Therefore, the flow around the cylindrical particles can be assumed to be axisymmetric and two-dimensional (2D) without flow separation, which is a valid assumption when the Reynolds number is less than 3.2 [24]. Therefore, the particle-resolved simulation was carried out in the 2D domain.

The details of the methodology for the RP approach can be found in Section 2.2. The details of the methodology for the PP approach is discussed in Section 2.3.

2.2. Resolved-particle approach

The following assumptions and simplifications were used for the simulations;

1. the particle is an infinitely long cylinder and consists only of ash-free carbon (no impurities),
2. the bulk fluid flow entering the simulation domain consists of only nitrogen (N_2) and carbon dioxide (CO_2),
3. the solid particle is stationary,
4. the local porosity is increasing with the progress of the reaction,
5. the fluid is incompressible (variable density condition was used),
6. the gas and solid phases inside the particle are in local thermal equilibrium ($T_g = T_s$), and
7. radiative absorption in the gas phase is neglected (i.e., particles exchange radiation directly with the reactor wall).

Inside the particle, the fluid flow follows the Navier–Stokes equation with a resistance due to the existence of the solid phase. The resistance is calculated using Darcy–Forchheimer law [25,26]. Further details of the equations can be found in the following section.

2.2.1. Governing equations outside the particle

The continuity equation is given by

$$\frac{\partial \rho_g}{dt} + \nabla \cdot (\rho_g \vec{u}) = 0, \tag{3}$$

where ρ_g is gas phase density and $\vec{u}$ is the velocity of the gas phase. Momentum conservation gives:

$$\frac{\partial (\rho_g \vec{u})}{dt} + \nabla \cdot (\rho_g \vec{u}\vec{u}^T) = -\nabla p + \nabla \cdot \mu[\nabla \vec{u} + \nabla \vec{u}^T - \frac{2}{3}(\nabla \cdot \vec{u})\vec{I}], \tag{4}$$

where p is pressure, μ is dynamic viscosity, and $\vec{I}$ is the identity matrix. The energy conservation equation reads as

$$\frac{\partial (\rho_g c_{p,g} T)}{dt} + \nabla \cdot (\rho_g c_p \vec{u} T) = -\nabla \cdot \lambda_g \nabla T, \tag{5}$$

where c_p is specific heat capacity of gas, T is temperature, and λ_g is thermal conductivity. Models used for estimation of all the thermophysical and transport properties are shown in Supplementary Materials (section S1). The gas species equation reads as

$$\frac{\partial (\rho_g Y_i)}{\partial t} + \nabla \cdot (\rho_g \vec{u} Y_i) = -\nabla \cdot (D_{eff,i} \nabla Y_i), \tag{6}$$

where Y_i is mass fraction of gas species i and $D_{eff,i}$ is effective diffusion coefficient of gas component i. The calculation of $D_{eff,i}$ can be found in Supplementary Materials (section S2).

2.2.2. Governing equations inside the particle

The model was derived based on the recommendation given in [22]. Since the solid phase inside the particle is stationary, the continuity and momentum conservation equations are solved only for the gas phase, while the volume occupied by the solid phase is accounted for by the local porosity. Hence, the continuity equation reads as:

$$\frac{\partial (\epsilon \rho_g)}{dt} + \nabla \cdot (\rho_g \vec{u}) = R_C, \tag{7}$$

where ϵ ($= V_g / V_{cell}$) is the local porosity of a cell in the computational domain, with V_g as the volume of the gas and V_{cell} as the total volume of the cell. R_C is the char gasification rate due to the Boudouard reaction (in kg m^{-3} s^{-1}). The momentum equation for the gas phase inside a porous medium is given by

$$\frac{\partial (\epsilon \rho_g \vec{u})}{\partial t} + \nabla \cdot (\rho_g \vec{u}\vec{u}^T) = -\nabla p + \nabla \cdot \mu[\nabla \vec{u} + \nabla \vec{u}^T - \frac{2}{3}(\nabla \cdot \vec{u})\vec{I}] - F_d, \tag{8}$$

where

$$F_d = \frac{\mu}{K}\vec{u}, \tag{9}$$

is the momentum transfer calculated based on Darcy–Forchheimer law [25,26] and

$$K = \frac{d_{pore}^2 \epsilon^3}{150(1-\epsilon)^2}, \tag{10}$$

is the permeability as given by the Carman–Kozeny equation with an average pore diameter d_{pore} [3,27].

A single energy equation can be used for the gas and solid phases due to the assumption of local thermal equilibrium of the two phases (see assumption 6):

$$\frac{\partial[\epsilon\rho_g c_{p,g} + (1-\epsilon)\rho_s c_{p,s}]T}{\partial t} + \nabla\cdot(\rho_g c_{p,g}\vec{u}T) = \nabla\cdot(\lambda_{eff}\nabla T) + \dot{Q}_{rad,p} + \dot{Q}_s, \tag{11}$$

where $c_{p,s}$ is specific heat capacity of solid, ρ_s is the true density of char and λ_{eff} is the effective thermal conductivity calculated as:

$$\lambda_{eff} = \epsilon\lambda_g + (1-\epsilon)\lambda_s. \tag{12}$$

The radiative exchange between the reactor wall and the external particle surface is given by

$$\dot{Q}_{rad,p} = \sigma\alpha(T_w^4 - T_p^4), \tag{13}$$

where σ is Stefan–Boltzmann constant, α is the emissivity of char, T_w is wall temperature and T_p is particle surface temperature. This term is zero for the internal cells. Furthermore, the enthalpy change due to the solid phase reaction reads as

$$\dot{Q}_s = \Delta H R_C, \tag{14}$$

where ΔH is the reaction enthalpy. The char reaction rate is expressed through the char conversion rate as

$$R_C = (1-\epsilon_0)\rho_s\frac{\partial X_C}{\partial t}, \tag{15}$$

where the char conversion rate reads as

$$\frac{\partial X_C}{\partial t} = k_c p_{CO2}^n . f(X_C). \tag{16}$$

Here, k_c is the rate constant and expressed as:

$$k_c = A\exp\left(-\frac{E_A}{RT}\right), \tag{17}$$

where A is the pre-exponential factor, E_A is the activation energy and p_{CO2} is the partial pressure of CO_2. Meanwhile, $f(X_C)$ is the conversion function. Following the random pore model, the conversion function is given by

$$f(X_C) = \frac{S_g}{S_{g,0}} = (1-X_C)\sqrt{1-\psi\ln(1-X_C)} \tag{18}$$

where S_g and $S_{g,0}$ are the instantaneous and initial local specific surface areas of the char particle, respectively, and ψ is the structure parameter of the random pore model. The local porosity, ϵ, is related to the char conversion, X_C, via

$$\epsilon = \epsilon_0 + X_C(1-\epsilon_0), \tag{19}$$

where ϵ_0 is the initial porosity of the char.

The gas species equation reads as

$$\frac{\partial(\epsilon\rho_g Y_i)}{\partial t} + \nabla\cdot(\rho_g\vec{u}Y_i) = -\nabla\cdot(Y_i\rho_g\overrightarrow{v_i^c}) + \nu_i R_C, \tag{20}$$

where Y_i is mass fraction of gas species i, ν_i is stoichiometric coefficient in the Boudouard reaction related to species i, and v_i^c is diffusion velocity of gas species i. The calculation of v_i^c can be found in Supplementary Materials (section S2).

The RP approach commonly imposes particle shrinkage by removing the remaining solid reactant of each cell at predetermined local conversion or porosity due to the impractically long computation time for the final stage of the conversion [19,22]. In this paper, the reaction rates of heterogeneous reactions were evaluated until the local porosity of each cell reached 0.99. At this point, the corresponding cell was considered to have reached complete conversion and all the remaining carbon was removed from the cell. When this happened the cell type was changed from porous material to pure gas phase.

Table 2
Common parameters used for all the simulation cases.

Type	Parameter	Value	Unit
Char	ρ_c	1200	kg m^{-3}
	λ_c	0.13	W m^{-2} s^{-1}
	$c_{p,c}$	1500	J kg^{-1} s^{-1}
	ϵ_0	0.7917	–
	τ_0	1.2632	–
	d_{pore}	250×10^{-9}	m
	ψ	1	–
Reaction kinetics [28]	E_A	2.62×10^5	J mol^{-1}
	A	1.19×10^9	s^{-1}MPa^{-n}
	n	0.46	–
	ΔH_0	17.78×10^5	J kg^{-1}
Radiation	α	0.8	–

2.2.3. Boundary conditions and initial conditions

The simulation domain is shown in Fig. 2. The domain has the following boundaries: *inlet*, *outlet*, *slip wall*, and *symmetry*. At the *inlet* boundary, all the physical, chemical, and transport properties are uniform across the boundary, except for pressure, where the Neumann boundary condition is used. The temperature is increased from room temperature (300 K) to reactor temperature within 10 ms, while the gas density is decreased accordingly. Neumann boundary condition is applied at the *outlet* boundary, except for pressure where a specific value is defined. *Slip wall* boundary condition is used on the upper wall of the domain where the surface normal velocity is zero. At the *symmetry* plane, the velocity normal to the boundary is zero, and all the other properties have Neumann boundary conditions.

The initial velocity and pressure fields were obtained based on isothermal simulation results at room temperature (300 K). Initial conditions, boundary conditions and dimensionless numbers for the cases are shown in Table 1. Other constant parameters that are common for all the cases are listed in Table 2, based on the literature data summarized in Supplementary Materials (section S3). Hereafter, the cases with higher η means cases 4–6 in Table 1 and cases with lower η means cases 1–3 in Table 1.

2.2.4. Numerical code validation and solution procedure

Simulations were carried out with the finite volume computational fluid dynamics (CFD) code OpenFOAM v6 [29] with our own numerical solver based on the governing equations described above. The Pressure-Implicit with Splitting of Operators (PISO) algorithm was used for the pressure–velocity coupling. All the finite volume differential schemes used were second-order accurate. The details about the validation, mesh refinement and domain size selection of the simulation model are presented in Supplementary Materials (section S4).

2.2.5. Estimation of effectiveness factors

The effectiveness factor can be calculated as follows based on the RP approach:

$$\eta_{real} = \frac{\Sigma\left[k_{c,cell}p_{CO_2,cell}^n f(X_{cell})dV\right]/V_p}{k_{c,s-av}p_{CO_2,s-av}^n f(X_{avg})}, \tag{21}$$

where $s-av$ is values based on averaging over the outer surface of the particle, dV is the volume of a mesh and V_p is the volume

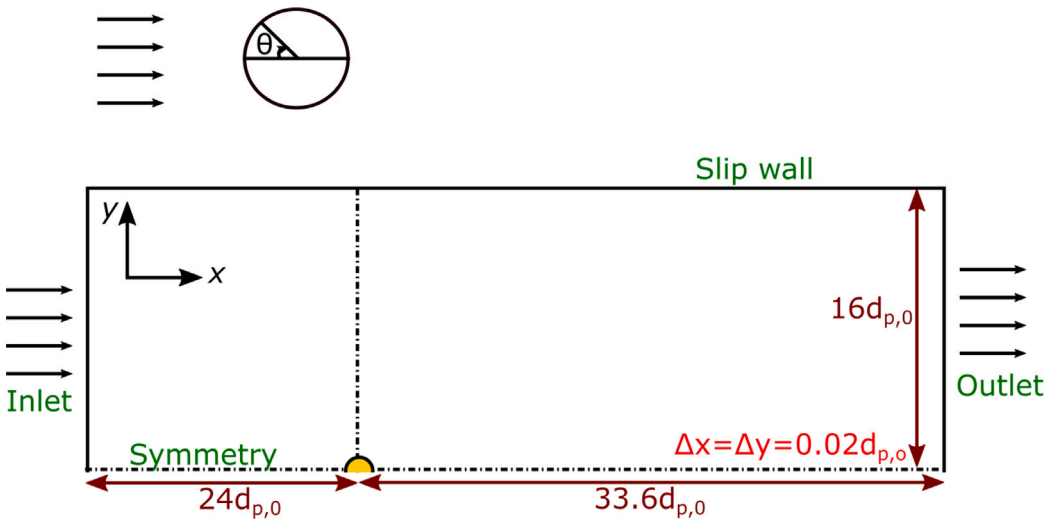

Fig. 2. The schematic image of the computational domain with the boundary condition, domain size, and mesh size. Here $d_{p,0}$ is diameter of the cylindrical particle, and Δj is the size of the mesh in direction j.

of the particle. When it is important to know only the effect of gas composition, we can calculate η as follows:

$$\eta_{CO_{2,based}} = \frac{\Sigma\left[k_{c,s-av} p^n_{CO_2,cell} f(X_{avg}) dV\right]/V_p}{k_{c,s-av} p^n_{CO_2,s-av} f(X_{avg})}. \tag{22}$$

2.3. Point particle approach

Unlike the resolved-particle (RP) approach, the point-particle (PP) approach does not consider the variation of properties such as temperature and gas composition inside the particle. The following sections describe the detail of the model using the PP approach.

2.3.1. Conservation of enthalpy and mass of the particle

Enthalpy of the particle varies due to diffusion of heat in the boundary layer (convective heat transfer), radiative heat transfer with the walls of the reactor, enthalpy changes due to the Boudouard reaction, advective heat transfer due to the Stefan flow and enthalpy transfer due to diffusion of gas species (Dufour effect), such that the particle temperature evolution is given by:

$$[\epsilon\rho_g c_{p,g} + (1-\epsilon)\rho_c c_{p,c}] V_p \frac{dT_p}{dt} = hA_p(T_\infty - T_p) + \sigma\alpha A_p(T_w^4 - T_p^4) - R_C \Delta H - Q_{Sf} - Q_{Dufour}, \tag{23}$$

where h is heat transfer coefficient, A_p is the external surface area of the particle, and T_∞ and T_w are far-field gas and wall temperature. The heat of reaction is temperature dependent and expressed as:

$$\Delta H = \Delta H_0 + \sum_i (\nu_{i,\mathrm{Boud}} \frac{W_i}{W_C} \int_{T_0}^{T_p} c_{p,i}\, dT), \tag{24}$$

where ΔH_0 is the heat of reaction at the standard temperature, ν_i is the stoichiometric coefficient of species i, W_i is the molar mass of species i, W_C is the molar mass of char and T_0 is temperature at standard condition. The advective transport of heat by the Stefan flow is expressed as:

$$Q_{Sf} = R_C \frac{W_{g,T_p}}{W_C} \int_{T_0}^{T_p} c_{p,g} dT_p, \tag{25}$$

where W_g is molar mass of gas mixture. The Dufour term is the enthalpy transfer due to gas species diffusion to/out of the particle;

$$Q_{Dufour} = \sum_i max\left\{0, h_{m,i}(C_{i,p} - C_{i,\infty}) A_p \int_{T_0}^{T_p} cp dT\right\} - \sum_i max\left\{0, h_{m,i}(C_{i,\infty} - C_{i,p}) A_p \int_{T_0}^{T_\infty} cp dT\right\} \tag{26}$$

where $h_{m,i}$ (see Eq. (36) for details) is the mass transfer coefficient of gas species i, and $C_{i,p}$ and $C_{i,\infty}$ are gas concentration of species i at particle surface and far-field, respectively.

The mass fraction of gas species inside the particle was calculated from the species balance considering convective mass transfer, consumption or generation by reactions, and advective transport by Stefan flow as:

$$\epsilon\rho_g V_p \frac{dY_{i,p}}{dt} = h_{m,i} W_i A_p (C_{i,\infty} - C_{i,p}) + \nu_{i,\mathrm{Boud}} \frac{W_i}{W_C} R_C - M_{i,Sf}, \tag{27}$$

where $h_{m,i}$ is the mass transfer coefficient of species i on a molar basis, C_i is the concentration of species i, and the advective transport of species by the Stefan flow is given by:

$$M_{i,Sf} = \left(\sum_i \nu_{i,\mathrm{Boud}}\right) R_C \frac{W_{g,p}}{W_C} Y_{i,p}. \tag{28}$$

2.3.2. Heat and mass transfer coefficients

Heat transfer coefficient without the effect of Stefan flow was calculated by:

$$h_0 = \mathrm{Nu}\lambda_{g,\infty}/d_p, \tag{29}$$

where the Nusselt number was calculated based on Whitaker [7] as:

$$\mathrm{Nu} = (0.4\mathrm{Re}_\infty^{\frac{1}{2}} + 0.06\mathrm{Re}_\infty^{\frac{2}{3}})\mathrm{Pr}_\infty{}^{0.4}(\frac{\mu_\infty}{\mu_p})^{\frac{1}{4}}. \tag{30}$$

Reynolds and Prandtl numbers were calculated from:

$$\mathrm{Re}_\infty = \frac{\rho_\infty U_\infty d_p}{\mu_\infty}, \tag{31}$$

and

$$\mathrm{Pr}_\infty = \frac{c_{p,\infty}\mu_\infty}{\lambda_\infty}, \tag{32}$$

where subscript ∞ represents the gas properties based on far-field conditions and p based on particle conditions.

Mass transfer coefficient without the effect of Stefan flow was calculated by:

$$h_{m0,i} = \frac{D_{iN_2}\mathrm{Sh}_i}{d_p}, \tag{33}$$

in m s^{-1}, and D_{iN2} is the binary diffusion coefficient between N_2 and species i. The Sherwood number is also calculated based on the Whitaker model:

$$\mathrm{Sh}_i = (0.4\mathrm{Re}_\infty^{\frac{1}{2}} + 0.06\mathrm{Re}_\infty^{\frac{2}{3}})Sc_{i,\infty}^{0.4}(\frac{\mu_\infty}{\mu_p})^{\frac{1}{4}}, \tag{34}$$

where Schmidt number was calculated from:

$$\mathrm{Sc}_{i,\infty} = \frac{\mu_\infty}{\rho_\infty D_{iN_2,\infty}}. \tag{35}$$

Parameters with sub-script ∞ are calculated based on temperature (T_∞), CO_2 mass fraction ($Y_{CO_2,\infty}$), and CO mass fraction ($Y_{CO,\infty}$), all at far-field conditions.

The effects of Stefan flow were considered for both heat and mass transfer coefficients as [30]:

$$h_i = h_{0i} \cdot \frac{\phi_{Stf,i}}{e^{\phi_{Stf,i}} - 1}, \tag{36}$$

where the correction term for the heat transfer coefficient was calculated as:

$$\phi_{Stf,th} = \frac{1}{h_0} \frac{R_C c_{p,g}}{\pi d_p}, \tag{37}$$

and that for mass transfer coefficient was calculated as:

$$\phi_{Stf,mass,i} = \frac{\dot{n}_{total}}{h_{0,mass,i}}, \tag{38}$$

where

$$\dot{n}_{total} = \frac{R_C}{W_C A_p} \left(\sum_i \nu_{i,\mathrm{Boud}} \right). \tag{39}$$

2.3.3. Reaction rate

The rate of carbon consumption by the Boudouard reaction, R_C in kg s^{-1}, is calculated from the particle conversion, X_p, the initial void fraction of the particle, ϵ_0, the true density of char, ρ_c, and the volume of the particle, V_p, as:

$$R_C = \frac{dm_c}{dt} = (1-\epsilon_0)\rho_c V_p \cdot \frac{dX_p}{dt}. \tag{40}$$

The conversion rate considers the effects of intra-particle diffusion via the effectiveness factor as [28,31]:

$$\frac{dX_p}{dt} = \eta \cdot k_c \cdot p^n_{CO_2,p} \cdot f(X_p), \tag{41}$$

where η is the effectiveness factor and $p_{CO_2,p}$ is the partial pressure of CO_2 at the particle surface. The same Arrhenius type expression as the RP approach (Eq. (17)) was applied for the rate constant, k_c. The structure-function, representing the change of the specific surface area from the initial value is given by:

$$f(X_p) = \frac{\rho_p}{\rho_{p,0}} \sqrt{1 - \psi \log\left(\frac{\rho_p}{\rho_{p,0}}\right)}. \tag{42}$$

The effectiveness factor for the cylinder particles can be calculated as:

$$\eta = f_c \frac{1}{\phi} \cdot \frac{I_1(2\phi)}{I_0(2\phi)}, \tag{43}$$

where f_c is the correction factor as suggested in [32] and $I_i(a)$ is the modified Bessel function of ith kind [33]. The Thiele modulus, ϕ, is calculated as [33]:

$$\phi = \frac{d_p}{4} \sqrt{\frac{(n+1)}{2D_{e,CO_2}} \frac{k_c f(X_p) \rho_{char}(1-\epsilon_0)}{W_C} \frac{RT}{p_{CO_2}}}, \tag{44}$$

where D_e is the effective diffusion coefficient of the porous particle. Calculation of D_e is shown in Supplementary Material (section S2).

2.3.4. Variation of particle diameter and density

The particle diameter remains constant until the conversion at the surface of the particle is converted to a critical value when the particle is considered to be completely consumed. The time when particle diameter starts to change (τ) can be then evaluated as the moment when $X_s = \overline{\eta}$ [20]. Therefore, the surface conversion is calculated in parallel through the integration of the local conversion rate at the particle surface as:

$$\frac{dX_s}{dt} = k_c \cdot p^n_{CO_2,p} \cdot f(X_s). \tag{45}$$

Once X_s reached critical conversion (95% in this study), the particle size is calculated based on [20]:

$$\frac{dr_p}{dt} = \frac{dm_p}{dt} \frac{1-\eta}{2\pi r_p \rho_p}, \tag{46}$$

where the particle density is calculated as:

$$\frac{d\rho_p}{dt} = \frac{dm_p}{dt} \frac{\eta}{\pi r_p^2}. \tag{47}$$

2.3.5. Calculation procedures

After deciding the time step for the point-particle calculations, temperature and gas species mass fractions were calculated using Eq. (23) and (27). Then all the time-varying parameters were calculated using the Euler-explicit method at each time step. The more detailed sequence of point-particle calculations can be found in Supplementary Material (section S5). The point-particle results were compared with volume-averaged parameters from particle-resolved simulations for the 6 cases in Table 1.

3. Results and discussion

3.1. Comparison of the point-particle and resolved-particle approaches

Simulation results from the point-particle (PP) approach and resolved-particle (RP) approach were compared with respect to particle diameter (d_p), particle temperature (T_p), gas composition ($Y_{i,p}$), char conversion (X_p), char conversion rate ($\frac{dX_p}{dt}$) and the effectiveness factor (η). The data from the RP approach were averaged over the entire particle volume (volume-averaged) and over the external curved surface of the particle (surface-averaged). Changes in particle diameter from the RP approach were evaluated as the average distances between the initial centre of the particle and the surface at the front, side, and back of the particle. It should be noted that cases 1–3 have lower η values (0.2–0.4) than cases 4–6 (0.6–0.7). Here, we call the cases 1–3 as "low η cases" and the cases 4–6 as "high η cases".

Fig. 3 shows char conversion plotted against time and char conversion rate plotted against char conversion for all the cases as a comparison between the RP approach and the PP approach. All the cases show a significant difference between the two approaches. The predictions by the PP approach and the RP approach are closer to each other in high η cases (Fig. 3(c)) than in low η cases (Fig. 3(a)). Moreover, the PP approach underestimates conversion rates for high η cases while it overestimate the conversion rates for low η cases. It indicates the existence of at least two sources of errors in the PP approach.

Another interesting observation is that the deviation of the PP approach from the RP approach is most profound for cases 1 and 4. The common properties of case 1 and case 4, apart from the particle Reynolds number, are high ratios of Stefan Reynolds number to particle Reynolds number ($\mathrm{Re}_{Sf}/\mathrm{Re} \approx 0.16$–$0.18$). The ratios for the other cases were $\mathrm{Re}_{Sf}/\mathrm{Re} \approx 0.007$–$0.013$, which is one order of magnitude lower than for cases 1 and 4.

Fig. 4 shows the effectiveness factor plotted against char conversion. The effectiveness factor of the RP approach is calculated as the local reaction rates integrated over the particle volume divided by the volume-integrated reaction rate obtained if the temperature, mass fractions of gas species, and particle conversion inside the particle were equal to the surface-averaged values (see Eq. (21) for more details). It clearly depicts that the PP approach overestimates the effectiveness factors. The relative differences become more pronounced for lower η cases. This explains the overestimation of the conversion rate by the PP approach at low η cases as it directly affects the conversion rates as shown in Eq. (41). Several potential reasons exist for overestimating the effectiveness factors in the PP approach. Firstly, the PP approach does not consider the change of temperature inside the particle, even though it considers mass diffusion resistance. Reactions in this study

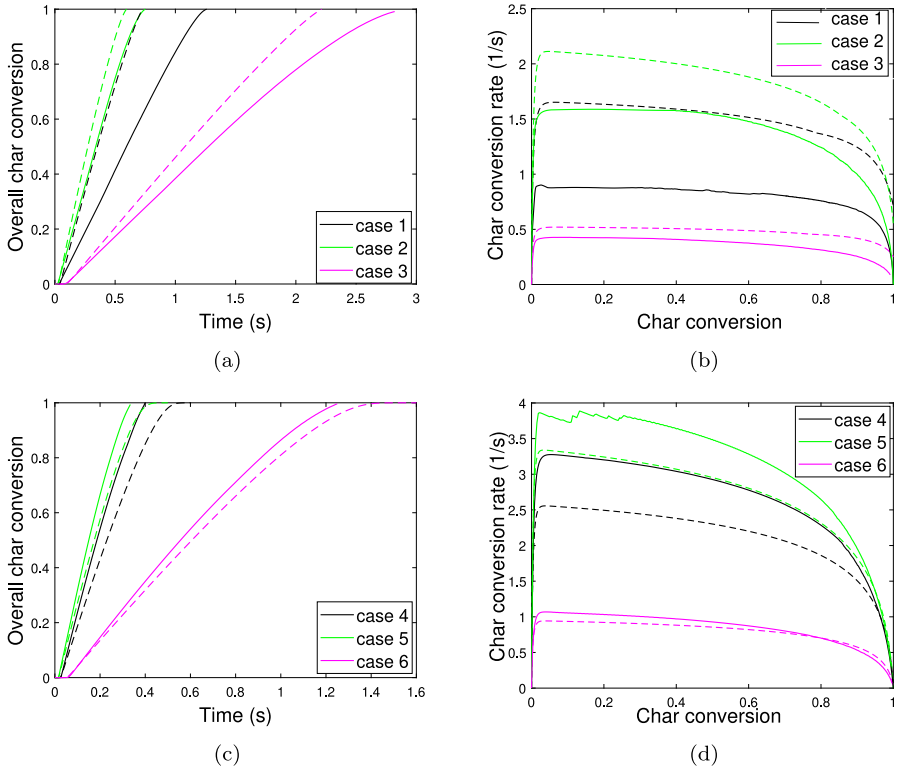

Fig. 3. Time vs. char conversion (a and c) and char conversion vs. conversion rate (b and d). Solid lines — RP approach; Dashed lines — PP approach.

are endothermic, and this can lower the internal particle temperatures. Therefore, in reality, the effectiveness factor can be significantly lower than calculated by the PP approach, where a uniform temperature is assumed. Secondly, the effectiveness factor in the PP approach was developed based on the mass diffusion through quiescent gas inside the pores. In reality, the non-equimolar reactions create a net outgoing flow, which can increase the diffusion resistance.

In order to elaborate more on the effect of temperature gradient inside the particle, we make the following thought experiment: Assume two particles that are identical, except that the thermal conductivity is finite for one of them while it is infinite for the other. Let us call the former, which will have an internal temperature gradient, p1, while the latter, which has uniform temperature, is named p2. Furthermore, assume that the reactions are equimolar, such that there is no Stefan flow, and that the relative velocity between the particles and the surrounding flow is negligible. Finally, let us choose parameters such that the overall char conversion rate is the same for p1 and p2. For endothermic reactions it is now clear that we have the following temperature relations:

$$T_\infty > T_{p1,s} > T_{p2,s} = T_{p2,c} > T_{p1,c}, \tag{48}$$

where subscripts s and c refer to the surface and the centre of the particle, respectively, while T_∞ is the far-field temperature. Since $T_{p1,s} > T_{p2,s}$, the reaction rate at the surface of p1 is higher than that of p2. Based on our assumption that the char conversion rates are the same for the two particles, the char conversion rate in the particle interior must therefore be slower for p1 than for p2. From the definition of effectiveness factor, this immediately implies that the effectiveness factor of p1 is lower than that of p2. Since the PP approach with the Thiele model implicitly implies an infinite thermal conductivity, this supports the explanation for the difference in effectiveness factors between the RP and PP approaches given in the paragraph above.

Now, let us relax the assumption that the char conversion rate of the two particles is the same. Note that this does not change the fact that the surface temperature of a particle with infinite thermal conductivity is underestimated compared to a particle with finite conductivity. For endothermic reactions, heat transfer to the particle is crucial in order to maintain the conversion rate. Since the heat transfer rate to the particle is proportional to the temperature gradient in the boundary layer surrounding the particle, the lower surface temperature of the particle with infinite conductivity results in a higher heat transfer rate. We know from the above that this particle also has an overestimated effectiveness factor. The result of this (high heat transfer and high effectiveness factor) is a higher char conversion rate, which is indeed what we observe for the PP approach.

As previously discussed in our studies [19,20], the errors in the estimations of the effectiveness factor may result in errors in particle size prediction. Fig. 5 compares the change of particle diameter at different char conversions from the PP approach and the RP approach. The onset of particle shrinkage in the PP approach was much later in char conversion than in the RP approach. This is reasonable because the PP approach overestimated the effectiveness factors (Fig. 4), which delays the start of shrinkage with respect to char conversion [19,20].

Fig. 6 shows the normalized particle temperature, $\theta = T_p/T_\infty$, as a function of char conversion. The temperature is normalized because each case has a different far-field temperature. The volume-averaged temperature was calculated based on the temperature field over the particle of the RP approach. All the data show a similar general trend; the particle temperature quickly rose to around 90% of the far-field temperature and slowly increased toward the far-field temperature at the later stage of the conversion. In all the cases, the particle temperatures from the PP approach are lower than those from the RP approach. The difference was more significant for the cases with low η, which tend to have higher temperature differences inside the particle. The results clearly show that the heat of reaction was large enough to affect the particle temperature. The difference in the particle temperature is quite important for the estimation of conversion rate as it is very sensitive to the temperature (Eq. (17)). In fact, conversion rates of the high η cases from the PP approach are lower than the RP approach (Fig. 3(d)) despite overestimating the effectiveness factors by two-fold (Fig. 4(b)).

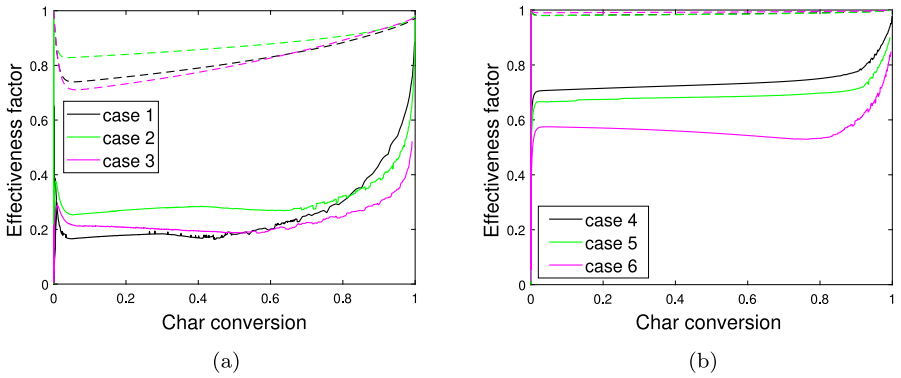

Fig. 4. Effectiveness factor variation as a function of char conversion for low η cases (a) and high η cases (b). Solid lines — RP approach; Dashed lines — PP approach.

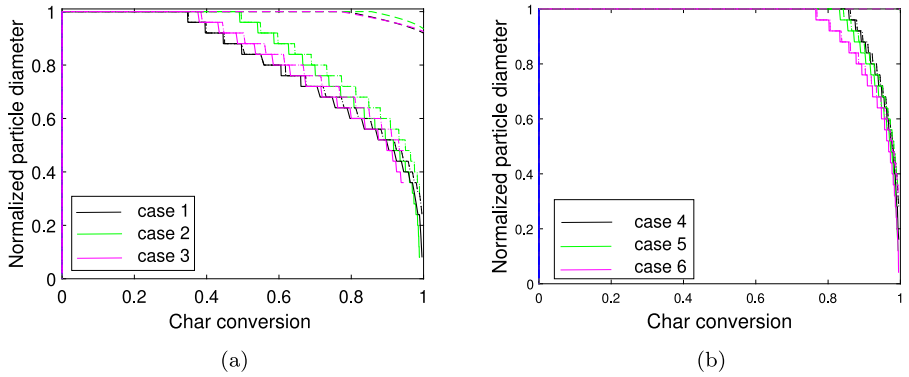

Fig. 5. Normalized particle diameter variation with char conversion for low η cases(a) and high η cases (b). Solid lines — RP approach; Dashed lines — PP approach. The diameter is normalized with the initial diameter of each case. Each case has three plots based on the diameter variation of the front, side, and back of the particle. In the future, diameter is referred to as the average of the three diameters.

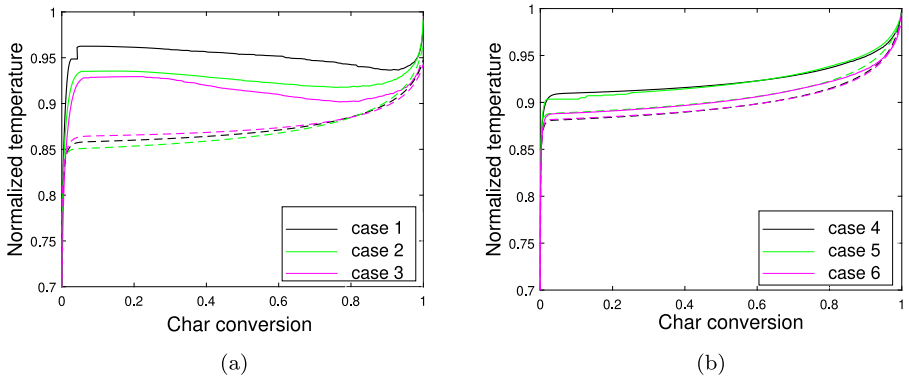

Fig. 6. Volume averaged temperature variation with char conversion. Solid lines — RP approach; Dashed lines — PP approach. Temperature is normalized with a far-field temperature of each case.

The effectiveness factor is calculated in the PP approach to account for the effects of mass diffusion resistance under the assumption that the particle temperature is uniform. To have a better understanding of the gasification conditions inside the particle, contour plots of temperature from the RP approach are studied. Fig. 7 shows the temperature contours for cases 1 and 4 at different char conversions. These cases have high $\mathrm{Re}_{Sf}/\mathrm{Re}$ ratios while case 1 has low η and case 4 has high η. It is apparent that temperature gradients within the particle are significant at all the conversion stages (X_p = 0.1–0.8) for both cases. In addition, case 1 (low η) shows asymmetric temperature distribution with the front side of the particle having lower temperature, indicating more intense reaction zones there. It is also an indication that the consumption of reactant gas (CO_2) at the front of the particle may affect the reactions at the back of the particle since most of the CO_2 is consumed in the front, leaving little to be used by the rear side. Such phenomena have not been considered even with three-dimensional particle models in recent studies [34] because the direction of bulk gas flows is not considered in such studies. Case 1 (Fig. 7(a)) exhibits about 50 K of temperature difference within the particle, and case 4 (Fig. 7(b)) about 70 K, which may cause the variation of local rate constant by 60–80%. All the cases in Table 1 have shown temperature differences close to or more than 50 K within the particle at X_p = 0.1–0.8. Temperature contours of the other 4 cases are presented in Supplementary Materials (section S6).

Fig. 8 shows the contours of CO_2 mass fraction (Y_{CO_2}) for the cases 1 (low η) and 4 (high η). It is very clear that CO_2 mass fraction inside the particle is close to zero for case 1. We could say that there is a strong diffusion resistance, and all the CO_2 that reaches the particle surface is

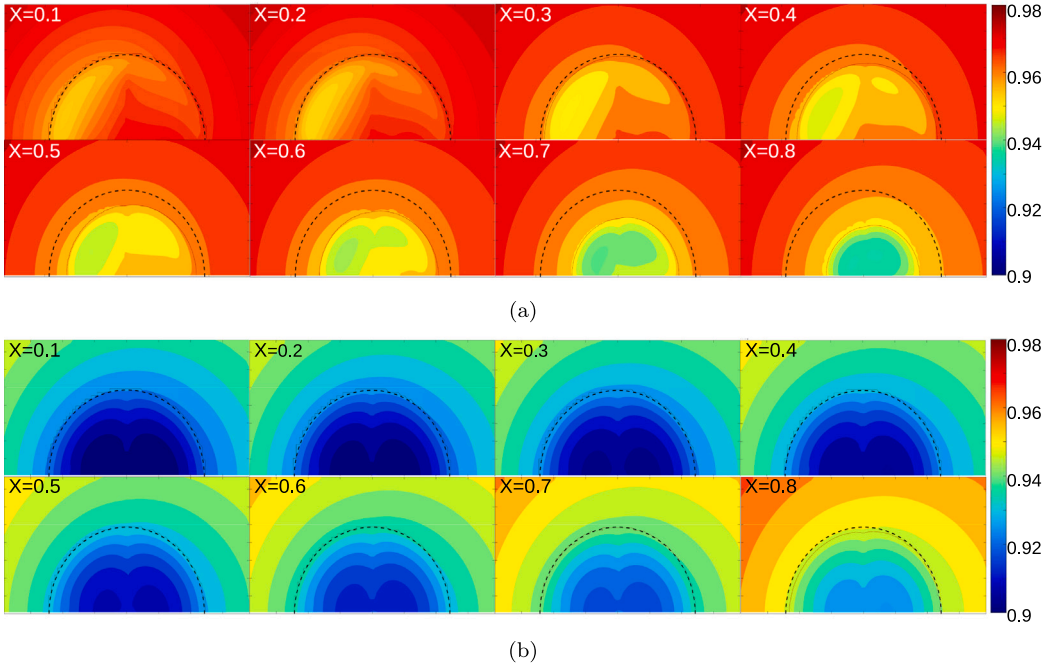

Fig. 7. Temperature contours of case 1 (a) and case 4 (b) of the normalized temperature (T/T_{∞}, where T is the temperature at each point of the particle surface). Both cases have similar Reynolds numbers. Case 1 has low values of effectiveness factor, and case 4 has high values.

consumed by reactions near the particle surface, which is similar to the zone III conditions. In fact, there is a low-temperature region near the particle surface (see Fig. 7) because of the heat of the reaction. To get more insight Fig. 9 shows CO mass fraction (Y_{CO}) contours for cases 1 and 4. CO (reaction product) is most likely generated near the external surface of the particle for case 1. The uniform CO distribution in case 1 shows that it has not only produced outward Stefan flow but also diffused inward and accumulated inside the particle.

Case 4 (high η) has non-zero but lower Y_{CO_2} inside the particle than at the particle surface. Hence, CO is most likely generated throughout the particle. The CO generated at the outer region of the particle may diffuse or advect outward from the particle and create a non-uniform Y_{CO} profile inside the particle.

The state-of-the-art models using the PP approach [22] assume (1) uniform temperatures within the particle, which did not happen in the RP approach for the cases simulated in this work. In addition, (2) effectiveness factor (η) correlations do not consider the convective effects due to reactions (Stefan flow) inside the particle. Finally, (3) the 3D effects (asymmetrical thermophysical parameters inside the particles) are not considered in the PP approach. These assumptions are potential sources of deviations between the results of the RP approach and the PP approach. In addition, the deviation of particle temperature between the RP approach and PP approach (see Fig. 6) throws doubt upon the accuracy of external heat transfer models. The next section is dedicated to studying possible deviations between the two approaches in detail.

3.2. Origins of deviations between the RP and PP approaches

Simulations with the point-particle approach (PP approach) applies various sub-models and assumptions. Simulation with the resolved particle approach (RP approach) eliminates many of the models. Instead, the RP approach resolves the particle interior and the boundary layer in a numerical mesh and use this to directly solve relevant evolution equations. This approach is much closer to reality than the PP approach. Therefore, the results from the RP approach can be used to identify the sources of inaccuracies of the PP approach. When used to model a reacting particle with a Stefan flow, the potential sources of error can be listed as follows based on findings of the previous section and by studying the PP equations:

1. 3D/2D asymmetry within the particle due to the effects of external flows
2. non-uniform temperature within the particle
3. neglecting the effects of convective flow inside the particle (Stefan flow)
4. external heat and mass transfer from/to the particle

In order to gain insights into these potential errors, we carried out a set of simulations with the following procedures to test the significance of some of the uncertainties:

1. RP approach with significantly higher thermal conductivity of char to eliminate non-uniform temperature within the particle,
2. PP approach using surface-averaged temperature from the RP approach results instead of solving Eq. (23) to examine the effects of the uncertainty in external heat transfer models,
3. PP approach using surface-averaged Y_{CO_2} from the RP approach results instead of solving Eq. (27) to examine the effects of deviations due to external mass transfer models of CO_2,
4. PP approach using both surface-averaged temperature and Y_{CO_2} from the RP approach results to examine the uncertainty in internal particle phenomena independent of external transport phenomena, except for the effects of the 3D asymmetry

Remaining uncertainties, such as the effects of intraparticle convective flow due to Stefan flow and 3-D/2-D asymmetry due to the interaction between internal and external phenomena, were considered to be outside the scope of this work. Instead, they will be addressed in future work by comparing the results with, for example, 1D particle models. The above 4 tests were carried out for case 4 (high η case with highest $\mathrm{Re}_{Sf}/\mathrm{Re}$ ratio). Char conversion was plotted against time while other parameters such as conversion rate, effectiveness factor, normalized particle diameter, particle temperature, and CO and CO_2 mass fraction were plotted against char conversion.

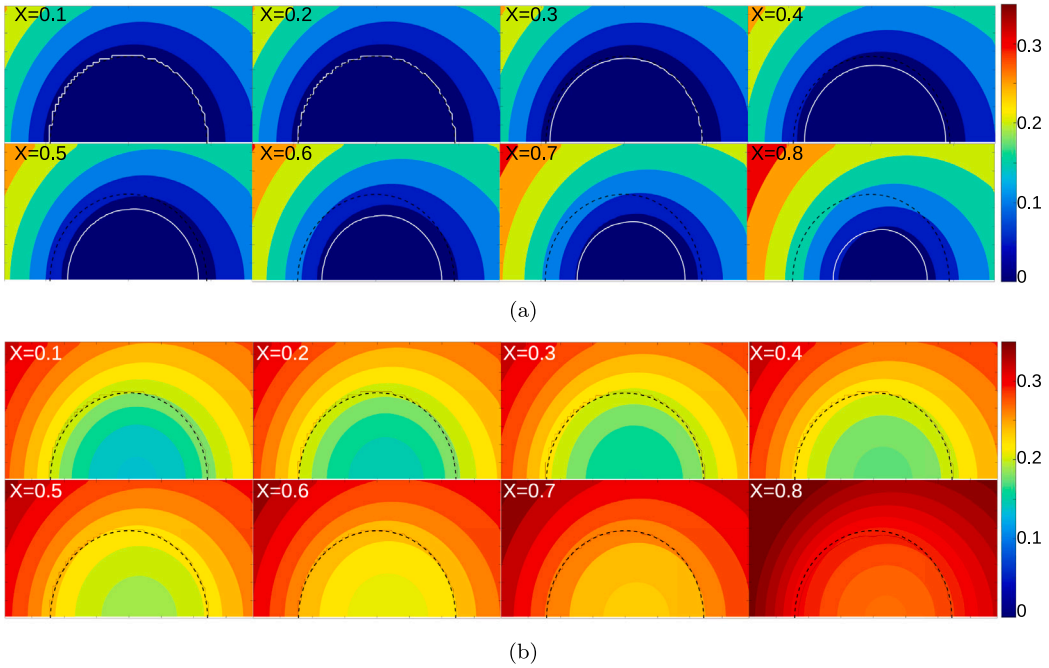

Fig. 8. CO_2 mass fractions contours of case 1 (a) and case 4 (b). Both cases have similar Reynolds numbers. Case 1 has low values of effectiveness factor, and case 4 has high values. White solid line in (a) indicates the particle surface during conversion and black dashed line indicates the initial particle diameter.

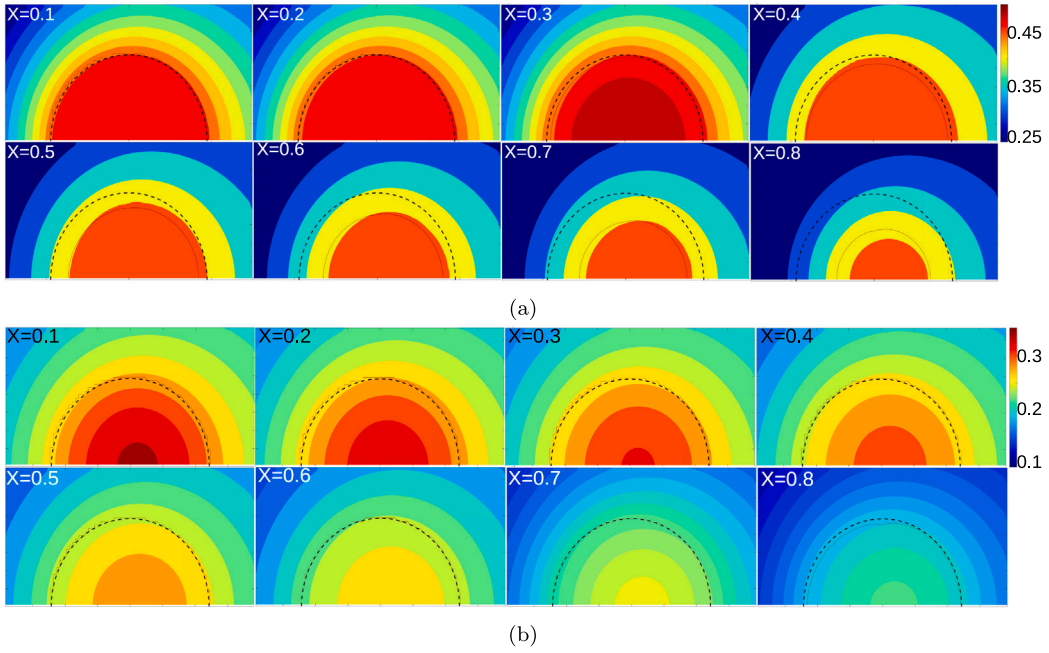

Fig. 9. CO mass fractions contours of case 1 (a) and case 4 (b). Both cases have similar Reynolds numbers. Case 1 has low values of effectiveness factor, and case 4 has high values.

3.2.1. *Non-uniform temperature inside the particle*

Figs. 10 and 11 show the comparisons between an ordinary RP approach, an RP approach with 100 times higher thermal conductivity of char, and a PP approach. The high conductivity RP approach resulted in an almost uniform temperature within the particle, which is in line with the underlying assumption of the PP approach. However, the conversion rates of the high conductivity RP approach (green-dashed-dot line in each figure) deviated more against the PP approach than the ordinary RP approach (black-solid line in each figure). The surface temperature of the ordinary RP approach is higher than the average particle temperature and reduces the external heat transfer rate. Therefore, the high conductivity RP approach gives higher surface-averaged particle temperature than the ordinary RP approach (see Fig. 11(a)). Meanwhile, the effectiveness factor of the ordinary RP approach based only on Y_{CO_2} (Eq. (22)) is slightly higher but comparable to that of the high conductivity RP approach. When the effects of the temperature are considered (Eq. (21)), the effectiveness factor of the ordinary RP approach becomes significantly lower than the high conductivity RP approach. Hence, the high conductivity RP approach results in a faster char conversion rate (see Figs. 10(a) and 10(b)).

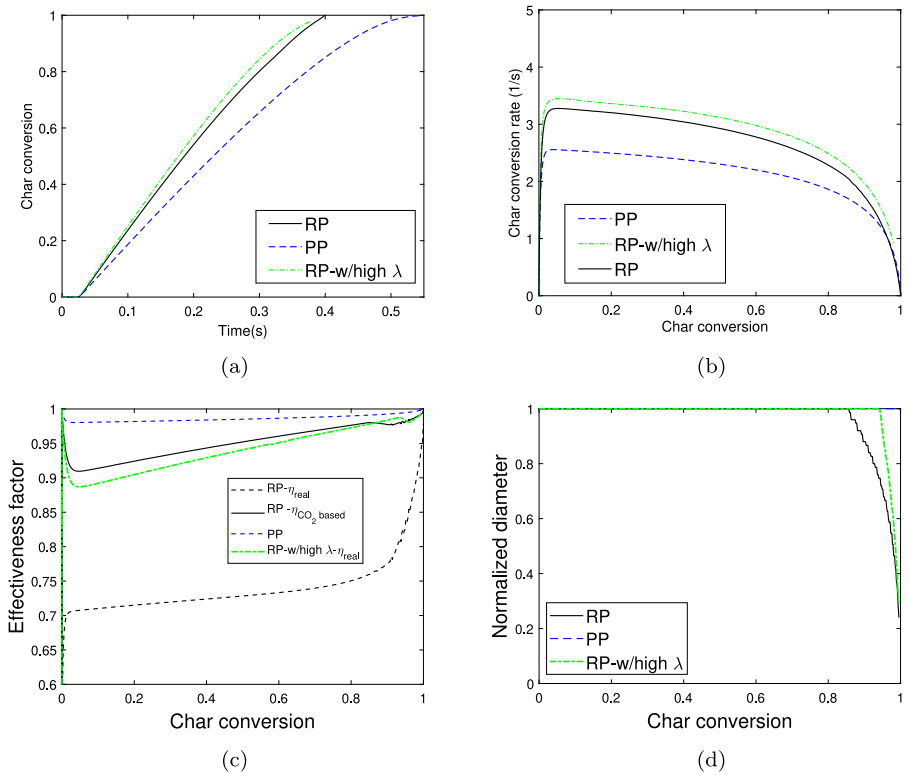

Fig. 10. Comparison of resolved-particle approaches (RP approach) with ordinary conductivity for char, RP approach with high conductivity for char, and point-particle approach (PP approach) for case 4. (a) Time vs. char conversion. (b) Char conversion vs. char conversion rate. (c) Char conversion vs. effectiveness factor. Black-dashed lines is η_{real} and black-solid line is $\eta_{CO_{2,based}}$ for RP approach (see Eqs. (21) and (22) for more details). (d) Char conversion vs. normalized particle diameter.

When looking closely at the particle temperature and mass fractions of CO_2 and CO for case 4 (Fig. 11), the PP approach underestimates the particle temperature and Y_{CO} while it overestimates Y_{CO_2}. The application of the high conductivity RP approach makes the deviation between the RP approach and the PP approach even larger. This means that, unlike for low-η cases, the temperature gradient inside the particle cannot be the main cause for the difference between the RP and PP approaches for the high-η case 4. Instead, the difference is probably more due to the effect of the particle-internal Stefan flow.

In summary, for high-η cases, uniform particle temperature assumption alone cannot explain the reason why the PP approach does not reproduce the conversion rates predicted from the RP approach. The two sources of errors, that is, the underestimation of external heat transfer rates and the uniform particle temperature assumptions, are most likely cancelling their effects on conversion rates. Therefore, the current test does not give an individual insight into the errors in external heat and mass transfer. The next section will look further at the performance of the PP approach when removing the inaccuracies of external heat and mass transfer models.

3.2.2. External heat transfer

When we use the average surface temperature obtained with the RP approach as boundary conditions for the PP approach — instead of solving the energy equation (Eq. (23)), we can remove the inaccuracies created from the errors in the model terms for external heat transfer. The terms in question are the heat transfer coefficient (h), the advective term due to Stefan flow (Q_{Sf}), and Dufour terms (Q_{Dufour}). Figs. 12 and 13 examine how the results from the PP approach improve by using the surface averaged temperature from the RP approach results.

The largest improvement is in gas mass fractions (see Figs. 13(b) and 13(c)) although it can simply be the coincidence, considering the large deviation in the prediction of char conversion (Fig. 12(a)). High consumption (overprediction) of the CO_2 and CO production in the particles is most likely compensated by the previously discussed overprediction of external mass transfer rates. When looking at particle temperature (Fig. 13(a)), the particle average temperature of the RP approach is slightly lower than that of the surface-averaged temperature used in the PP approach. The PP approach with the given surface temperature shows a comparable effectiveness factor (Fig. 12(c)) to that of the RP approach calculated only based on Y_{CO_2} variation. It is much higher than the effectiveness factor of the RP approach with the consideration of both temperature and mass fraction variations inside the particle. From these results, we can interpret that the deviation of the conversion rate mainly originates from the failure of the PP approach in considering the drop in the temperature inside the particle.

Then, questions about the external heat transfer rates arise. The inaccuracies must have originated from the errors in h, Q_{Sf}, or Q_{Dufour} unless the effects of 3D/2D asymmetry are significant. We can examine the contribution of terms Q_{Sf}, Q_{Dufour}, $M_{i,Sf}$ by removing them from Eqs. (23) and (27). The effect of the Nusselt number (Nu) can be examined by replacing model-based Nu with Nu calculated from the RP approach. Fig. 14 shows the volume-average temperature when the terms are removed (Q_{Sf}, Q_{Dufour}, $M_{i,Sf}$) or replaced by values from the RP approach (Nu). It shows that the effects of terms Q_{Sf}, Q_{Dufour}, $M_{i,Sf}$ are negligible compared to the effect of the Nusselt number. This can be seen from the improvement in the particle-averaged temperature by using Nu from the RP approach. We could say the rest of the deviation of the temperature could be due to hot gas entering the particle or additional unknown effects.

3.2.3. External mass transfer

As discussed in the previous section, the PP approach seems to overpredict mass transfer rates of CO_2. By eliminating the inaccuracy of external mass transfer rates, we can evaluate how errors of the PP approach in external heat transfer and uniform temperature assumption inside the particle compensate for each other. Hence, we compared the

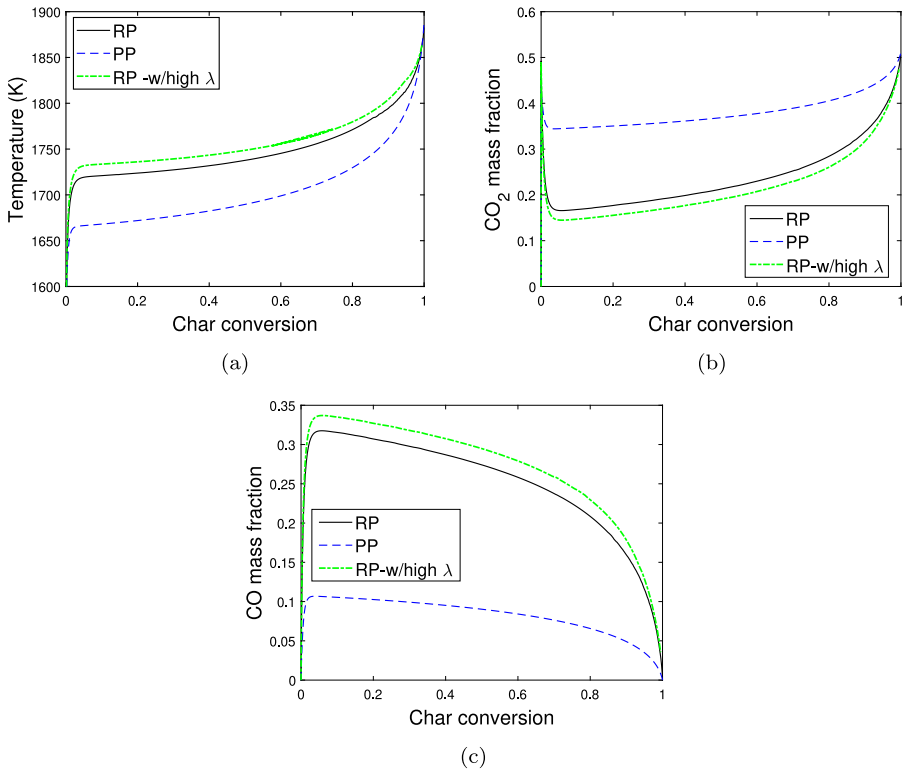

Fig. 11. Comparison of resolved-particle approaches (RP approach) with ordinary conductivity for char, RP approach with high conductivity for char, and point-particle approach (PP approach). (a) Char conversion vs. volume-averaged particle temperature. (b) Char conversion vs. CO_2 mass fraction. (c) Char conversion vs. CO mass fraction.

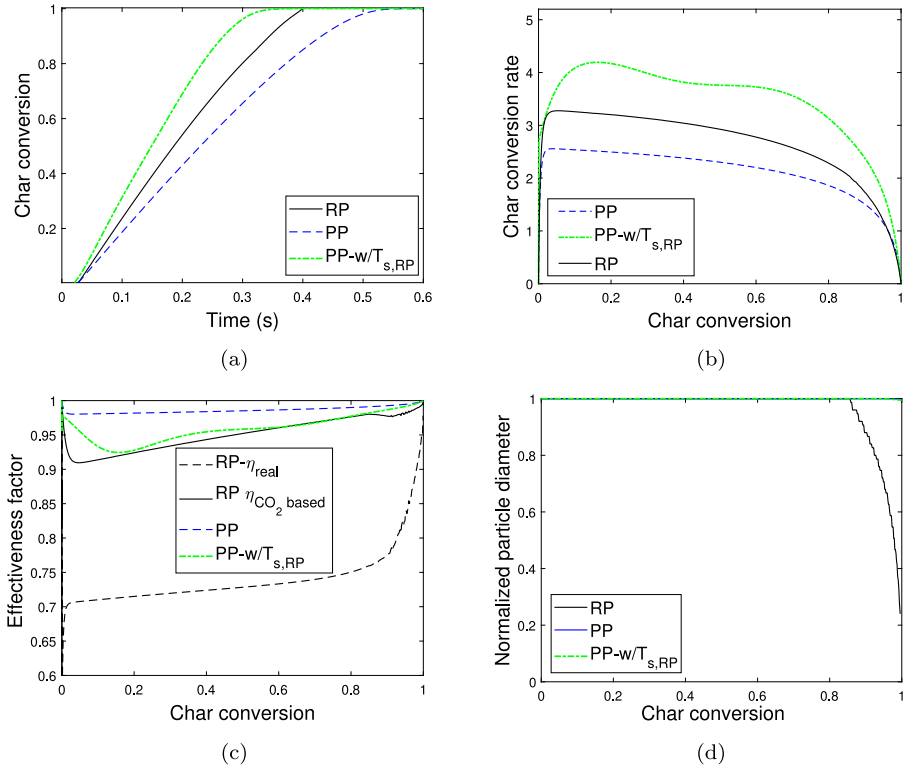

Fig. 12. Comparison of the resolved-particle approach (RP approach), the point-particle approach (PP approach), and the PP approach using average surface temperature from the RP approach instead of Eq. (23). (a) Time vs. char conversion. (b) Char conversion vs. char conversion rate. (c) Char conversion vs. effectiveness factor. Black-dashed lines is η_{real} and black-solid line is $\eta_{CO_{2,based}}$ for RP approach (see Eqs. (21) and (22)for more details). (d) Char conversion vs. normalized particle diameter.

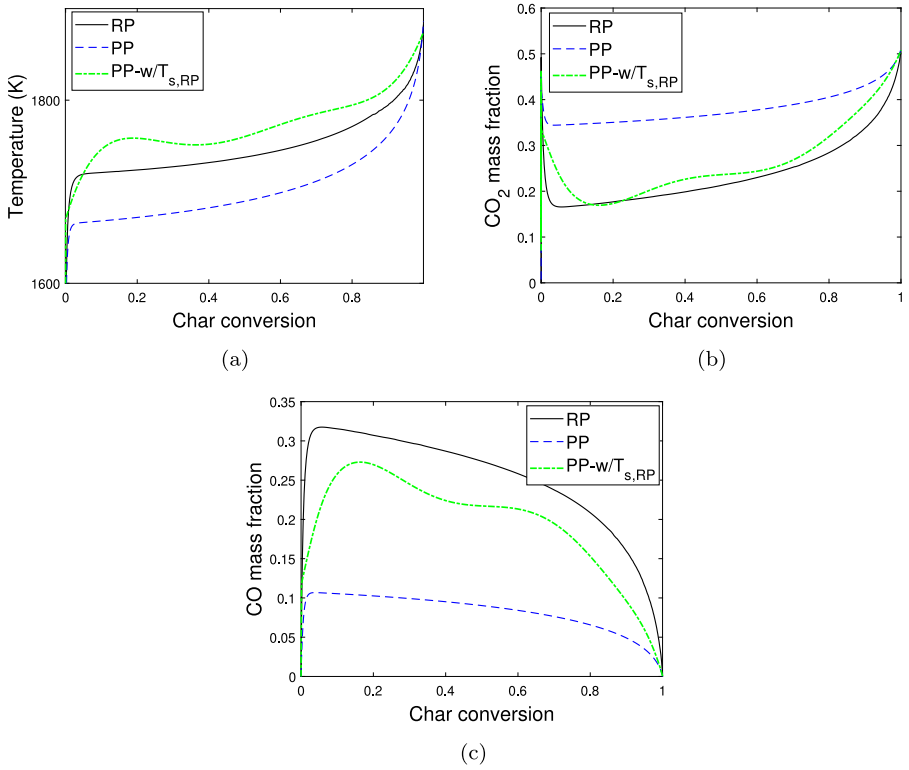

Fig. 13. Comparison of the resolved-particle approach (RP approach), the point-particle approach (PP approach), and the PP approach using average surface temperature from the RP approach instead of Eq. (23). (a) Char conversion vs. volume-averaged particle temperature. (b) Char conversion vs. CO_2 mass fraction. (c) Char conversion vs. CO mass fraction.

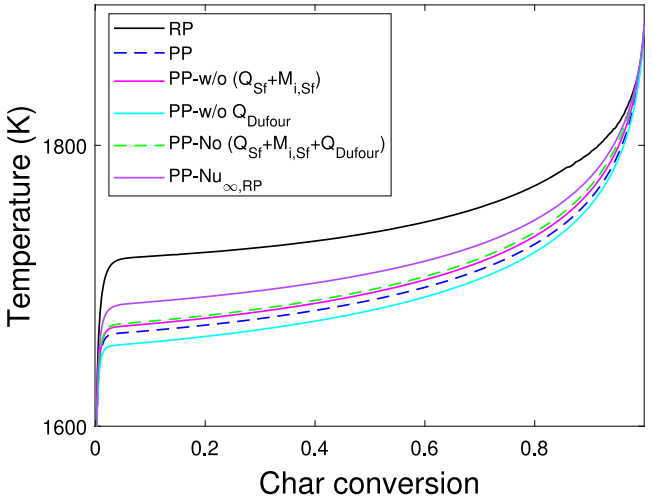

Fig. 14. Comparison of the particle temperature from resolved-particle approaches (RP approach) with point-particle approach (PP approach) using different approaches. The exclusions of heat and mass transfer by advection due to Stefan flow, PP-w/o (Q_{Sf}+$M_{i,Sf}$), the exclusion of Dufour term, PP-w/o Q_{Dufour}, and the use of Nusselt number extracted from the RP approach, PP-$Nu_{\infty,RP}$, in Eqs. (23) and (27) were considered.

PP approach and RP approach results with PP approach results using the surface-averaged mass fraction of CO_2 from the RP approach results instead of solving Eq. (27). Figs. 15 and 16 show the comparison of results from the RP approach and PP approach with the PP approach using given CO_2 mass fraction.

Instant observation is that the PP approach results with the given mass fraction of CO_2 show a very close char conversion rate and particle temperature to those from RP results. However, a large deviation from the RP approach remains for the effectiveness factor, CO gas composition, and particle size changes. The deviation of CO is relatively expected because overprediction of the mass transfer rates of CO is not adjusted in the model. The PP approach with the given mass fraction of CO_2 showed a higher effectiveness factor than the RP approach, while their conversion rates showed similar values. This is due to the compensation of the high effectiveness factor in the PP approach with non-uniform temperature in the RP approach. In conclusion, it is a coincidence that the reaction rates of the two simulation results show a negligible difference in this case. The difference in conversion rates may become apparent under different reaction conditions, especially at different effectiveness factors.

3.2.4. Intra-particle heat and mass transfer

When the PP approach is carried out by using both surface-averaged particle temperature and CO_2 mass fraction from the RP approach, we can eliminate the inaccuracy of external heat and mass transfers. The comparison of the PP approach results with such treatment with the RP approach results can highlight the inaccuracies in the intra-particle transport phenomena. Figs. 17 and 18 show the results of such simulation cases, *i.e.,* the PP approach using the pre-determined particle temperature and CO_2 mass fraction as surface averaged values in RP approach results.

The effectiveness factor from the PP approach shows a relatively similar value as the effectiveness factor of the RP approach based only on the variation of Y_{CO_2} inside the particle (*i.e.,* no consideration of the effects of the temperature or local conversion variation). Nevertheless, the effectiveness factor of the PP approach is slightly higher than that based on the Y_{CO_2} variation from the RP approach results. One potential reason for this deviation is the outward convective flow inside the particle. The effectiveness factor used in the PP approach was developed based only on mass diffusion and without convective flows from non-equimolar equations. When the real effectiveness factor of the RP approach is used as a reference, the difference becomes more

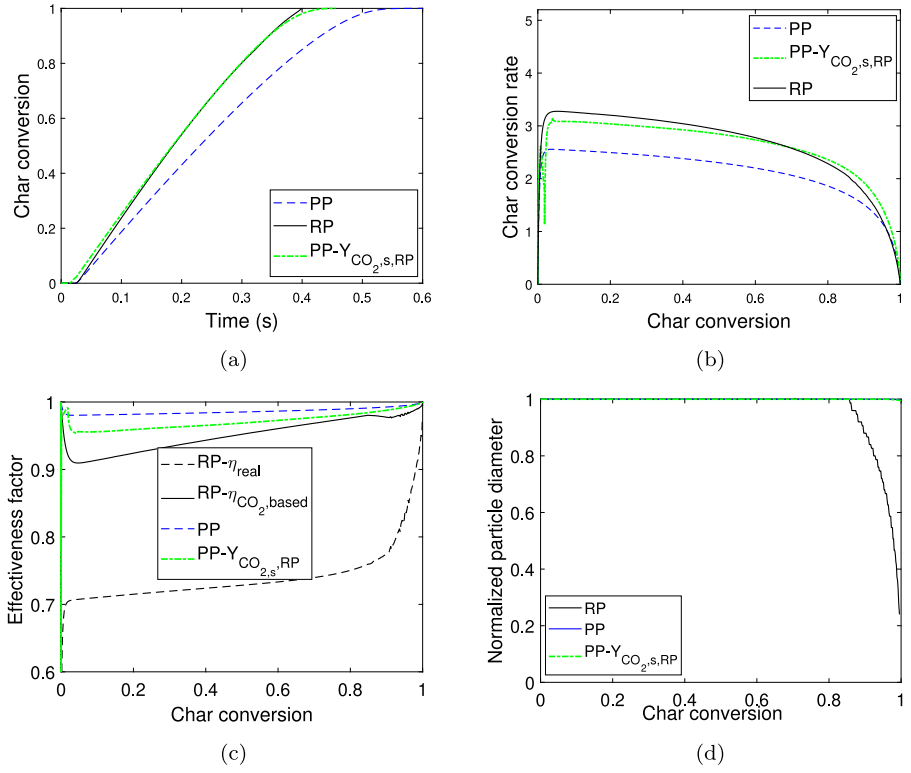

Fig. 15. Comparison of resolved-particle approaches (RP approach), point-particle approach (PP approach), and PP approach using the average surface mass fraction of CO_2 from RP approach instead of solving Eq. (27). (a) Time vs. char conversion. (b) Char conversion vs. char conversion rate. (c) Char conversion vs. effectiveness factor. Black-dashed lines is η_{real} and black-solid line is $\eta_{CO_{2,based}}$ for RP approach (see Eqs. (21) and (22) for more details). (d) Char conversion vs. normalized particle diameter.

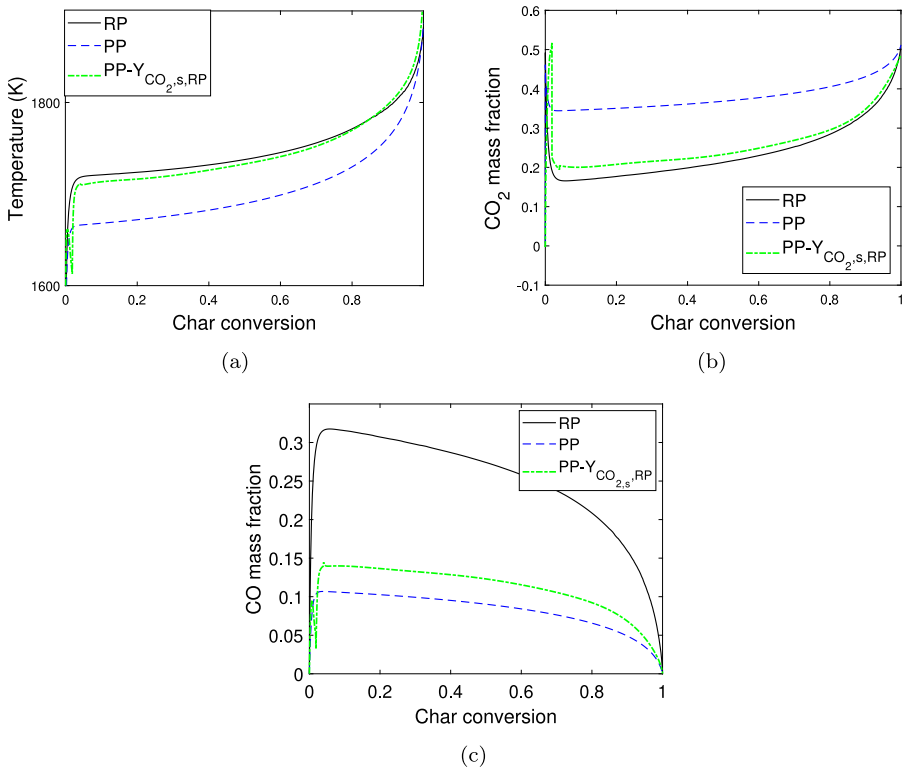

Fig. 16. Comparison of resolved-particle approaches (RP approach), point-particle approach (PP approach), and PP approach using the average surface mass fraction of CO_2 from RP approach instead of solving Eq. (27). (a) Char conversion vs. volume-averaged particle temperature. (b) Char conversion vs. CO_2 mass fraction. (c) Char conversion vs. CO mass fraction.

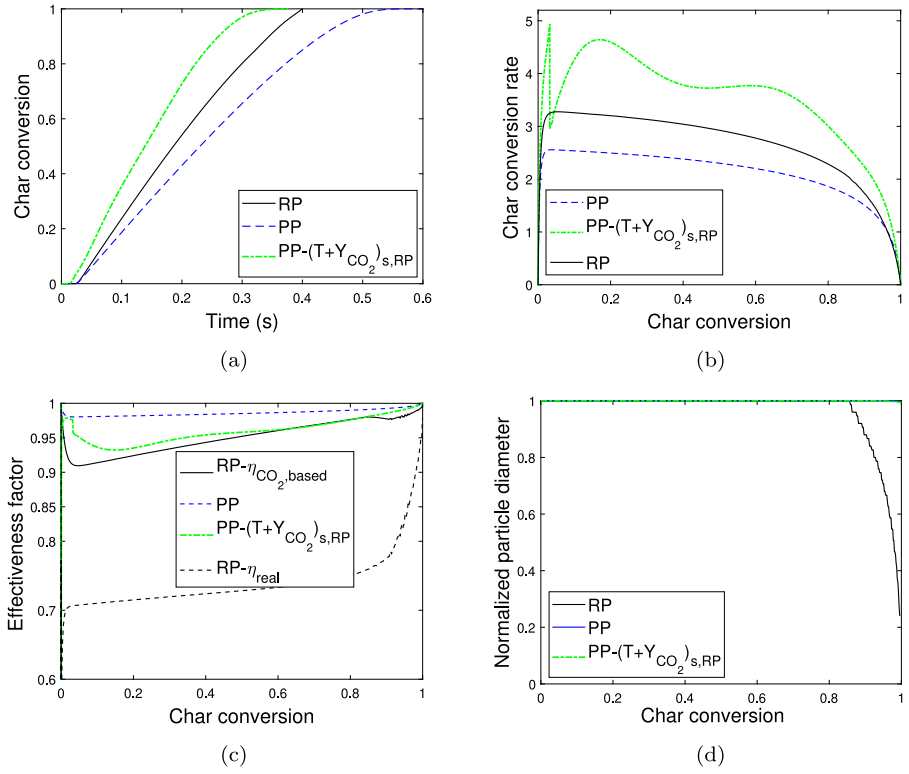

Fig. 17. Comparison of resolved-particle approaches (RP approach), point-particle approach (PP approach), and PP approach using the average surface mass fraction of CO_2 and average surface temperature from RP approach instead of solving Eqs. (23) and (27). (a) Time vs. char conversion. (b) Char conversion vs. char conversion rate. (c) Char conversion vs. effectiveness factor ($\eta_{CO_2,based}$). (d) Char conversion vs. normalized particle diameter.

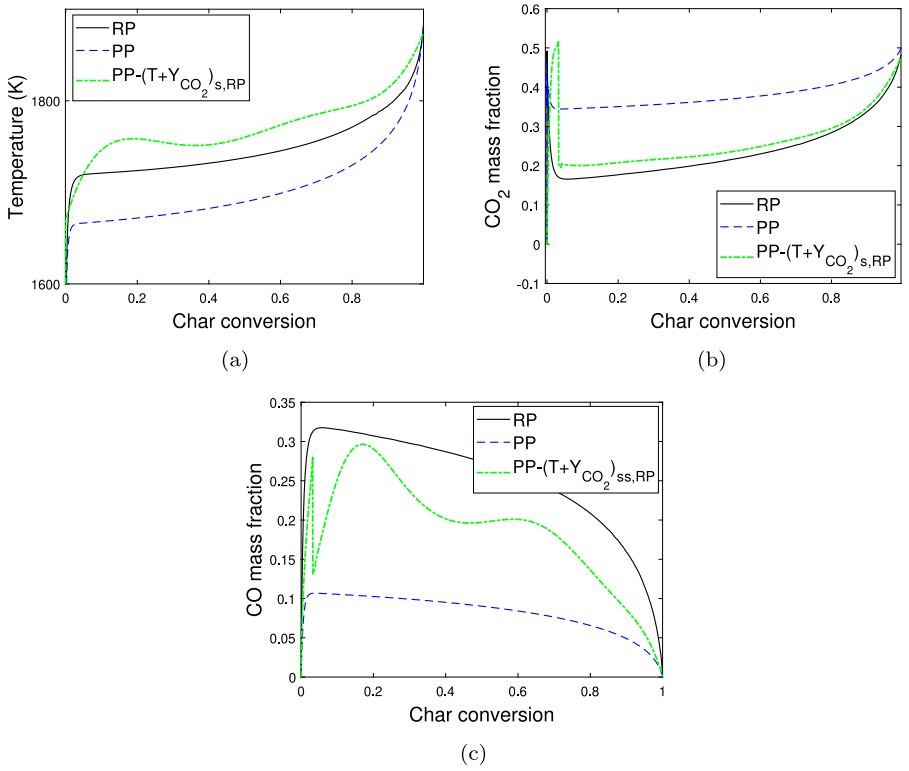

Fig. 18. Comparison of resolved-particle approaches (RP approach), point-particle approach (PP approach), and PP approach using the average surface mass fraction of CO_2 and average surface temperature from RP approach instead of solving Eqs. (23) and (27). (a) Char conversion vs. volume-averaged particle temperature. (b) Char conversion vs. CO_2 mass fraction. (c) Char conversion vs. CO mass fraction.

significant, which indicates that the effect of non-uniform temperature is larger than the effects of internal convective flows (η_{real} is not shown in Fig. 17(c)).

The PP approach results do not indicate any onset of the decrease in particle size for this condition. The point particle approach does not include the effect of the non-uniform temperature inside the particle. This intrinsic inaccuracy makes the effectiveness factor of the PP approach always deviate from that of reality (or the RP approach) as long as the heat of the reaction is not zero. Therefore, it is reasonable that the PP approach overestimates the critical conversion for the onset of particle shrinkage.

None of the tests discussed in Sections 3.2.2–3.2.4 did improve the prediction of variation in particle diameter. The main reason is probably the fact that the prediction of the real effectiveness factor from the PP approach is too high for this case. Another potential reason, which is unique for zone II conditions, is the inability of the PP approach to consider the variations of porosity inside the particles caused by earlier stages of reactions. When the effectiveness factor is significantly lower than unity, the porosity near the particle surface becomes higher than the particle core. Therefore, the inherent assumption of the effectiveness factor, that is, the uniform porosity inside the particles, increases the effectiveness factor at the later stage of conversion compared to the reality. This deviation can result in a delay in the onset of particle shrinkage by the PP approach.

According to Haugen et al. [20], the onset of particle diameter variation is predicted accurately by Eq. (46) when the particle interior temperature is uniform and the variation of parameters is one-dimensional. Results in this work show that the effectiveness factor from the PP approach and therefore the onset of particle diameter become inaccurate when the temperature of the particle interior is not uniform and affected by two-dimensional variation of parameters.

4. Conclusions

A series of simulations using the resolved particle and point particle approaches highlight a few important sources of inaccuracies in the point particle approach.

The dominant source of inaccuracies for the intra-particle heat and mass transfer is the effects of non-uniform temperature distribution, *i.e.,* lower particle temperature due to endothermic reactions. Since the effectiveness factor commonly applied in char conversion models do not consider the effects of non-uniform temperature, the PP approach always overestimates the effectiveness factor. The inaccuracy in predicting the effectiveness factor also results in the inability to predict the particle size changes.

When the inaccuracies of both external and internal heat and mass transfer are considered, the eventual outcome is dependent on the effectiveness factor because of the shift in their relative importance. When the effectiveness factors are relatively large (close to zone I conditions), the errors in external heat transfer dominate the overall conversion rates. When the effectiveness factors are smaller (near zone III conditions), the inaccuracy of using uniform particle temperature becomes more important, and the PP approach tends to overestimate the conversion rates. Interestingly, this study sheds light on a few occasions when one or more parameters from the PP approach results agreed very well with the RP approach, solely by the coincidence of two or more errors cancelling each other. It strongly suggests that the accuracy of the point particle approach must be examined thoroughly by comparing several parameters, preferably at a wide range of reaction conditions.

Other potential sources of errors, such as the 2D/3D asymmetry and intra-particle convective flows, were also identified. Future studies should include comprehensive comparisons of several different modelling approaches, such as the point particle approach, one-dimensional particle model, and multi-dimensional resolved-particle model with and without the direct solution of external flows.

CRediT authorship contribution statement

Thamali R. Jayawickrama: Data curation, Formal analysis, Investigation, Methodology, Software, Validation, Visualization, Writing – original draft. **Nils Erland L. Haugen:** Conceptualization, Funding acquisition, Methodology, Resources, Supervision, Writing – review & editing. **Kentaro Umeki:** Conceptualization, Funding acquisition, Investigation, Methodology, Project administration, Resources, Supervision, Writing – review & editing.

Declaration of competing interest

The authors declare the following financial interests/personal relationships which may be considered as potential competing interests: Kentaro Umeki reports financial support was provided by Swedish Research Council. Kentaro Umeki reports equipment, drugs, or supplies was provided by Swedish National Infrastructure for Computing. Nils Erland L. Haugen reports equipment, drugs, or supplies was provided by Norwegian Research Infrastructure Services. Nils Erland L. Haugen reports financial support was provided by Research Council of Norway. Nils Erland L. Haugen reports financial support was provided by EU horizon 2020. If there are other authors, they declare that they have no known competing financial interests or personal relationships that could have appeared to influence the work reported in this paper.

Data availability

Data will be made available on request.

Acknowledgements

The authors are grateful to the Swedish Research Council (Vetenskapsrådet) for financial support for the study (grant number: 2015-05588 and 2023-04185). The simulations were enabled by resources provided by the Swedish National Infrastructure for Computing (SNIC) at High-Performance Computing Center North (HPC2N), partially funded by the Swedish Research Council through grant agreement no. 2018-05973. We thank all the staff of HPC2N for their technical assistance. This work also benefited from computer resources made available through the Norwegian NOTUR program under the award NN9405K. N.E.L.H. acknowledge the Research project Gaspro, financed by the research council of Norway (267916) and the European Union's Horizon 2020 research and innovation program (No 764697). K.U. also thank the Federal Ministry of Education and Research (BMWF) for the funding of the project REDEFINE H2E (01DD21005).

Appendix A. Supplementary data

Supplementary material related to this article can be found online at https://doi.org/10.1016/j.fuel.2024.131743.

References

[1] Higman C, Burgt M. Gasification. Gulf Professional Publishing; 2008.
[2] Weiland F. Pressurized entrained flow gasification of pulverized biomass: experimental characterization of process performance (Ph.D. thesis), Luleå University of Technology; 2015.
[3] Nikrityuk PA, Meyer B, editors. Gasification processes: modeling and simulation. 1st ed. Wiley-VCH; 2014.
[4] Göktepe B. Entrained flow gasification of biomass soot formation and flame stability (Ph.D. thesis), Luleå University of Technology; 2015.
[5] Hasse C, Debiagi P, Wen X, Hildebrandt K, Vascellari M, Faravelli T. Advanced modeling approaches for CFD simulations of coal combustion and gasification. Prog Energy Combust Sci 2021;86:100938. http://dx.doi.org/10.1016/j.pecs.2021.100938.
[6] Schiller L, Naumann A. A drag coefficient correlation. Z Vereins Deutscher Ingenieure 1935;77:318–20.

[7] Whitaker S. Forced convection heat transfer correlations for flow in pipes, past flat plates, single cylinders, single spheres, and for flow in packed beds and tube bundles. AIChE J 1972;18:361–71. http://dx.doi.org/10.1002/aic.690180219.
[8] Ranz W, Marshall W. Evaporation from drops. Chem Eng Prog 1952;48(3):141–6.
[9] Chen Y, Jiang P, Xiong T, Wei W, Fang Z, Wang B. Drag and heat transfer coefficients for axisymmetric nonspherical particles: A LBM study. Chem Eng J 2021;424:130391. http://dx.doi.org/10.1016/j.cej.2021.130391.
[10] Sanjeevi SK, Kuipers JA, Padding JT. Drag, lift and torque correlations for non-spherical particles from Stokes limit to high Reynolds numbers. Int J Multiph Flow 2018;106:325–37. http://dx.doi.org/10.1016/j.ijmultiphaseflow.2018.05.011.
[11] Richter A, Nikrityuk PA. Drag forces and heat transfer coefficients for spherical, cuboidal and ellipsoidal particles in cross flow at sub-critical Reynolds numbers. Int J Heat Mass Transfer 2012;55(4):1343–54. http://dx.doi.org/10.1016/j.ijheatmasstransfer.2011.09.005.
[12] Ma H, Zhao Y. Convective heat transfer coefficient for a rod-like particle in a uniform flow. Int J Heat Mass Transfer 2020;147:118742. http://dx.doi.org/10.1016/j.ijheatmasstransfer.2019.118742.
[13] Nugraha MG, Andersson R, Andersson B. On the Sherwood number correction due to Stefan flow. Chem Eng Sci 2022;249:117292. http://dx.doi.org/10.1016/j.ces.2021.117292.
[14] Muto M, Yuasa K, Kurose R. Numerical simulation of ignition in pulverized coal combustion with detailed chemical reaction mechanism. Fuel 2017;190:136–44. http://dx.doi.org/10.1016/j.fuel.2016.11.029.
[15] Bai Y, Luo K, Qiu K, Fan J. Numerical investigation of two-phase flame structures in a simplified coal jet flame. Fuel 2016;182:944–57. http://dx.doi.org/10.1016/j.fuel.2016.05.086.
[16] Rieth M, Kempf AM, Kronenburg A, Stein OT. Carrier-phase DNS of pulverized coal particle ignition and volatile burning in a turbulent mixing layer. Fuel 2018;212:364–74. http://dx.doi.org/10.1016/j.fuel.2017.09.096.
[17] Luo K, Wang H, Fan J, Yi F. Direct numerical simulation of pulverized coal combustion in a hot vitiated co-flow. Energy Fuels 2012;26:6128–36. http://dx.doi.org/10.1021/ef301253y.
[18] Cai R, Luo K, Watanabe H, Kurose R, Fan J. Recent advances in high-fidelity simulations of pulverized coal combustion. Adv Powder Technol 2020;31(7):3062–79. http://dx.doi.org/10.1016/j.apt.2020.05.001.
[19] Kreitzberg T, Phounglamcheik A, Haugen NEL, Kneer R, Umeki K. A shortcut method to predict particle size changes during char combustion and gasification under regime II conditions. Combust Sci Technol 2022;194(2):272–91. http://dx.doi.org/10.1080/00102202.2019.1678919.
[20] Haugen NEL, Tilghman MB, Mitchell RE. The conversion mode of a porous carbon particle during oxidation and gasification. Combust Flame 2014;161:612–9. http://dx.doi.org/10.1016/j.combustflame.2013.09.012.
[21] Tilghman MB, Haugen NEL, Mitchell RE. Comprehensive Char Particle Gasification Model Adequate for Entrained-Flow and Fluidized-Bed Gasifiers. Energy Fuels 2017;31:2164–74. http://dx.doi.org/10.1021/acs.energyfuels.6b02148.
[22] Haugen NEL, Loong BKY, Mitchell RE. Numerical approaches for thermochemical conversion of char. Prog Energy Combust Sci 2022;91:100993. http://dx.doi.org/10.1016/j.pecs.2022.100993.
[23] García Llamas ÁD, Guo N, Li T, Gebart R, Umeki K. Rapid change of particle velocity due to volatile gas release during biomass devolatilization. Combust Flame 2022;238:111898. http://dx.doi.org/10.1016/j.combustflame.2021.111898.
[24] Tritton DJ. Experiments on the flow past a circular cylinder at low Reynolds numbers. J Fluid Mech 1959;6:547–67. http://dx.doi.org/10.1017/S0022112059000829.
[25] Tufano GL, Stein OT, Kronenburg A, Gentile G, Stagni A, Frassoldati A, et al. Fully-resolved simulations of coal particle combustion using a detailed multi-step approach for heterogeneous kinetics. Fuel 2019;240:75–83. http://dx.doi.org/10.1016/j.fuel.2018.11.139.
[26] Ranzi E, Faravelli T, Manenti F. Pyrolysis, Gasification, and Combustion of Solid Fuels. Adv Chem Eng 2016;49:1–94. http://dx.doi.org/10.1016/bs.ache.2016.09.001.
[27] Szekely J, Evans J, Sohn H. Gas-solid reactions. Academic Press; 1976.
[28] Kajitani S, Suzuki N, Ashizawa M, Hara S. CO2 gasification rate analysis of coal char in entrained flow coal gasifier. Fuel 2005;85:163–9. http://dx.doi.org/10.1016/j.fuel.2005.07.024.
[29] Weller HG, Tabor G, Jasak H, Fureby C. A tensorial approach to computational continuum mechanics using object-oriented techniques. Comput Phys 1998;12:620–31. http://dx.doi.org/10.1063/1.168744.
[30] Murphy JJ, Shaddix CR. Combustion kinetics of coal chars in oxygen-enriched environments. Combust Flame 2006;144:710–29. http://dx.doi.org/10.1016/j.combustflame.2005.08.039.
[31] Kajitani S, Zhang Y, Umemoto S, Ashizawa M, Hara S. Co-gasification reactivity of coal and woody biomass in high-temperature gasification. Energy Fuels 2010;24(1):145–51. http://dx.doi.org/10.1021/ef900526h.
[32] Hong J, Hecker WC, Fletcher TH. Improving the accuracy of predicting effectiveness factors for mth order and langmuir rate equations in spherical coordinates. Energy Fuels 2000;14(3):663–70. http://dx.doi.org/10.1021/EF9902193.
[33] Levenspiel O. Chemical reaction engineering. 3rd ed. John Wiley & Sons; 1999.
[34] Martí-Rosselló T, Li J, Lue L, Karlström O, Brink A. Comprehensive assessment of particle-scale modeling for biomass pyrolysis: One-dimensional versus three-dimensional models. Energy Fuels 2021;35(12):9937–49. http://dx.doi.org/10.1021/acs.energyfuels.1C00283.